technologies

MDPI

Article

Constructing Temperature Prediction Model for Preventing Deep Roadway Rockburst via Revealing the Thermo-Mechanical Coupling Mechanism of Rough Wall

Dan Chen [1], Lang Shi [1,2,*], Manqing Lin [2,3], Shouqing Li [4] and Yongxiong Lu [1,2,*]

[1] School of Optical Information and Energy Engineering, Wuhan Institute of Technology, Wuhan 430205, China; dan_chen2026@163.com
[2] Hubei Key Laboratory of Optical Information and Pattern Recognition, Wuhan Institute of Technology, Wuhan 430205, China
[3] School of Resources & Safety Engineering, Wuhan Institute of Technology, Wuhan 430205, China
[4] Hubei Xingfa Chemicals Group Co., Ltd., Yichang 443711, China
* Correspondence: lang_shi@wit.edu.cn (L.S.); luyx@wit.edu.cn (Y.L.)

Abstract

Deep roadway rockburst is affected by the coupled effects of temperature and stress. However, conventional thermo-mechanical coupling models generally neglect the effect of natural wall roughness, leading to inaccurate analysis of the thermal response for the surrounding rock mass. This hinders the construction of a high-precision temperature prediction model for preventing deep roadway rockburst. To address this issue, we propose a region-growing algorithm integrated with recursive subdivision and adaptive growing, which achieves high-precision segmentation of rock structural planes. A three-dimensional finite-element model combining realistic rough-wall geometry characteristics was further constructed. Thermo-mechanical coupling simulations were conducted under different ground stress levels. The results indicate that the rough walls alter local heat conduction paths, causing restricted heat dissipation and accumulation in concave zones while promoting efficient cooling in convex zones. As the ground stress increases, the stress field amplitude scales approximately linearly, while the local temperature rise and thermal gradients exhibit a nonlinear increment. We further construct a polynomial temperature prediction model with R^2 = 0.9819 and RMSE/span = 3.26%. Standardized coefficients show that equivalent stress is the strongest statistical correlate and dominant ranking factor of temperature response, while roughness further amplifies thermal anomalies by inducing localized stress concentrations. The thermo-mechanical framework demonstrates that roughness determines anomaly localization and stress controls thermal growth magnitude. This study provides a theoretical basis for the identification of infrared temperature anomalies and early warning of rockburst hazards in deep roadways.

Keywords: deep roadway rockburst; roughness; region-growing algorithm; thermal-mechanical coupling; temperature prediction model

Academic Editor: Frédéric Lebon

Received: 24 October 2026
Revised: 21 November 2026
Accepted: 23 November 2026
Published: 25 November 2026

Copyright: © 2026 by the authors. Licensee MDPI, Basel, Switzerland. This article is an open access article distributed under the terms and conditions of the Creative Commons Attribution (CC BY) license.

1. Introduction

With the increasing depth of mining engineering, rockburst disasters induced by the coupling effect of high geostress and high ground temperature have become increasingly

severe, which seriously threatens the construction safety and operation schedule of underground engineering projects [1–4]. Typical engineering cases include the Bayu Tunnel of the Sichuan–Tibet Railway (overburden depth of approximately 2080 m, with rockburst hazards affecting up to 94% of the tunnel length) and the Jinping-II headrace tunnel (overburden depth of approximately 2525 m, where intensive rock fragment ejection was observed) [5–7]. Rockburst is a dynamic failure phenomenon induced by the sudden release of mechanical strain energy during excavation unloading in deep rock masses [8]. The incubation and development process of rockbursts is dominated by the multi-physical coupling of stress, temperature, and damage fields, and remarkable thermal infrared radiation (TIR) anomalies can be detected before rock failure [9]. In recent years, numerous studies have focused on the triggering mechanisms of rockbursts under thermo-mechanical coupled conditions [10]. Rock fracture behavior can generate obvious high-temperature TIR precursors, which essentially reflect the temperature response characteristics of thermo-mechanical coupling. Specifically, high-temperature anomalous zones are always concentrated in stress concentration regions prior to rockburst occurrence in deep roadways [11–13]. Based on this fundamental principle, infrared thermal monitoring technology has been widely developed and applied as an effective method to identify thermal anomaly precursors corresponding to stress accumulation and microfracture nucleation in rock masses [14–16].

Infrared monitoring is widely used for rockburst early warning, yet most thermo-mechanical coupling studies only adopt intact rock or simplified fractures, neglecting natural structural plane roughness [11]. Surface roughness does not merely alter contact conditions; it also controls the spatial paths of heat flow and the local redistribution of stress. In fractured rock masses, roughness generates heterogeneous apertures, uneven contacts, and tortuous heat-flow pathways, which in turn affect thermal transport and the resulting thermal stress field. Sun et al. [17] conducted laboratory heating experiments on fractured granite with different fracture-surface roughness and initial stress states, and demonstrated that roughness and pre-existing stress jointly control the magnitude and localization of thermal stresses. Li et al. [18] further showed that the thermal contact resistance of granite joints evolves with normal stress, meaning that the same rough interface can exhibit different heat-transfer efficiencies depending on the stress state. These joint-scale studies indicate that roughness–stress coupling influences not only the mechanical response but also the thermal field of the surrounding rock; in parallel, laboratory and model-scale observations show that infrared high-temperature zones are spatially consistent with stress-concentrated zones [19] and that gently inclined structural planes govern the location and intensity of rockburst damage [20]. Meng et al. [21] further showed that irregular joint surfaces, together with elevated normal stress, increase both the likelihood and the intensity of slip rockbursts, a purely mechanical effect rather than a heat-generation mechanism. Since an exposed roadway wall is a free surface, no frictional contact pair exists and no shear-induced heat is generated. In this study, roughness is therefore treated as a morphology-mediated factor.

Accurate quantification of structural plane roughness is vital for applying roughness characteristics to rockburst risk assessment. Traditional contact measurement methods are low-efficiency for structural plane information extraction, whereas terrestrial laser scanning (TLS) rapidly acquires high-precision rock mass point clouds [22,23]. The region-growing algorithm segments point cloud asperities into individual patches but fails to balance segmentation accuracy and noise immunity for complex rock masses. To quantitatively characterize the roughness of these segmented surfaces, several approaches have been developed. Barton [24] proposed the subjective visual comparison-based joint roughness coefficient (JRC). Fractal theory provides a powerful tool to quantify 3D rock surface roughness [25]. Zhou et al. [26] extended fractal theory to the cubic covering method, and

the improved differential box-counting algorithms have been further refined to directly calculate the fractal dimension of structural plane roughness [27].

To overcome the neglect of real rough surfaces in thermo-mechanical coupling models, this study carries out three main works: (1) a recursive subdivision-adaptive region-growing algorithm is developed, which realizes high-precision segmentation of complex structural planes via plane-fitting verification and recursive re-segmentation; (2) thermo-elastic numerical simulations are conducted in ANSYS workbench 2022 R1 using a 3D roadway model with actual rough surfaces to explore the thermal response and stress distribution induced by morphology-mediated heat conduction; and (3) roughness is quantified via the box-counting method, and a roughness-dependent temperature–stress model is constructed to reveal roughness control mechanisms and offer theoretical guidance for safe mining of deep phosphate mines.

2. Information Extraction from Rough Wall

To construct a three-dimensional roadway finite-element model that captures real rough-wall surfaces, intelligent identification of rock mass discontinuities is required. The core task is to accurately identify and cluster points belonging to the same geometric plane from the 3D point cloud data and then extract key parameters such as orientation, spacing, and roughness. For this purpose, data preprocessing first employs voxel filtering for downsampling to reduce data volume while preserving geometric features. Moving least squares is then applied to smooth the point cloud, filter out noise, and reconstruct a smoothed surface representation.

2.1. Region-Growing Algorithm Combining Recursive Subdivision and Dynamic Adaptation

To address the trade-off between segmentation accuracy and noise robustness for multi-planar structures in complex rock mass point clouds, this study proposes an improved region-growing algorithm integrated with recursive subdivision and dynamic adaptation. As illustrated in Figure 1, the algorithm takes the raw point cloud P, initial smoothness threshold S_0 (normal angle threshold, set to 10°), initial curvature threshold C_0 (set to 0.2), and plane-fitting distance error threshold T (set to 0.03) as inputs, and finally outputs a series of segmented plane clusters $\{P_1, P_2, ..., P_m\}$. The detailed implementation procedures are presented in Figure 1.

- Normal estimation: Compute the normal vector for each point in P using a k = 10 nearest-neighbor search;
- Initial region growing: Run the conventional region-growing algorithm with the initial thresholds $(S, C) = (S_0, C_0)$. Neighboring points satisfying the normal angle condition angle < S_0, curvature condition < C_0, and connectivity criteria are merged into the same region, yielding a set of initial clusters $\{C_1, C_2, ...\}$;
- Plane fitting and adaptive refinement: For each initial cluster, fit a plane using the least squares method. If the fitting error exceeds the distance threshold T, the region is considered to exhibit overall undulation or discontinuity. In this case, the growing criteria are dynamically tightened: the smoothness threshold is reduced to ($S = S_0 - 0.2$) and the curvature threshold to ($C = C_0 - 0.001$), and region growing is performed again within that cluster to separate finer adjacent planes or subtle discontinuities;
- Termination and result output: When a cluster can no longer be effectively subdivided or no longer meets the recursion conditions, it is sorted and, following a deduplication check to avoid overlap with previously output planes, added to the final segmentation result set $\{P_1, P_2, ..., P_m\}$.

By dynamically and adaptively tightening the thresholds, the proposed algorithm significantly improves boundary accuracy in segmentation while maintaining the integrity of large planes.

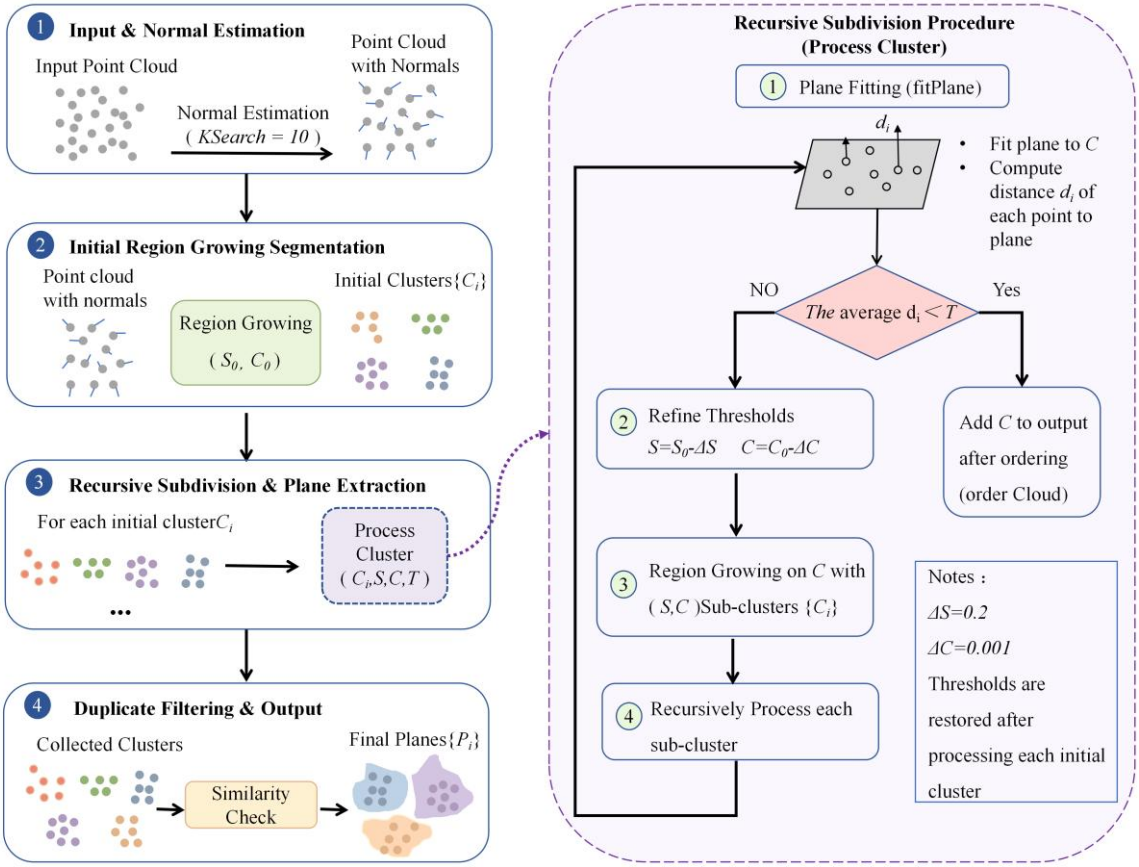

Figure 1. Flowchart of the improved region-growing algorithm.

2.2. Application of the Improved Region-Growing Algorithm in a Mine Roadway

This investigation targets a deep phosphate deposit buried at ~500 m in Xingshan County, Yichang, Hubei Province. The deposit is hosted in dolomite surrounding rocks, with stratified ore bodies dominated by phosphorite. A Livox-Mid-70 LiDAR was adopted to acquire 3D morphological data of roadway sidewalls, with a scanning frequency of 100,000 points/s and measurement accuracy better than 2 cm. Real-time data transmission and storage were realized based on the Robot Operating System (ROS), yielding point cloud datasets in standard PCD (Point Cloud Data) format. The scanning coverage on the XZ projection plane reaches 5.67 m × 3.16 m (Figure 2a). Structural plane segmentation was performed via the proposed improved region-growing algorithm, with critical parameters set as follows: smoothness threshold = 10°, curvature threshold = 0.2, region-growth similarity threshold = 0.03. A parametric study was performed to examine the influences of S, C, and T. As shown in Figure 2, both the smoothness threshold S (8~12°) and curvature threshold C (0.10~0.30) exhibit stable plateaus in plane counts. The region-growth threshold T (0.02~0.05 m) controls the recursive depth. The selected parameters (S = 10°, C = 0.20, T = 0.03 m) are located at the optimal balance point (1021 planes), ensuring both high coverage and robustness against noise.

Segmentation results from the conventional and proposed algorithms are displayed in Figure 3b,c, where distinct colors represent independent point clusters. Comparative analysis reveals that the developed algorithm accurately extracts large continuous structural planes while greatly improving recognition precision for angular irregular edges,

including fracture junctions and segmentation boundaries. This method eliminates the under- and over-segmentation defects of conventional algorithms at complex boundaries and improves its capacity to capture structural geometric features alongside anti-noise robustness in complicated geological environments. To quantitatively validate this improvement, the spatial coverage rate was calculated. As shown in Figure 3d, the proposed algorithm achieves a spatial coverage rate of 95.05% at a voxel size of 0.03, significantly outperforming the conventional algorithm (72.78%). This quantitatively proves that the proposed method effectively eliminates under-segmentation and captures large continuous structural planes.

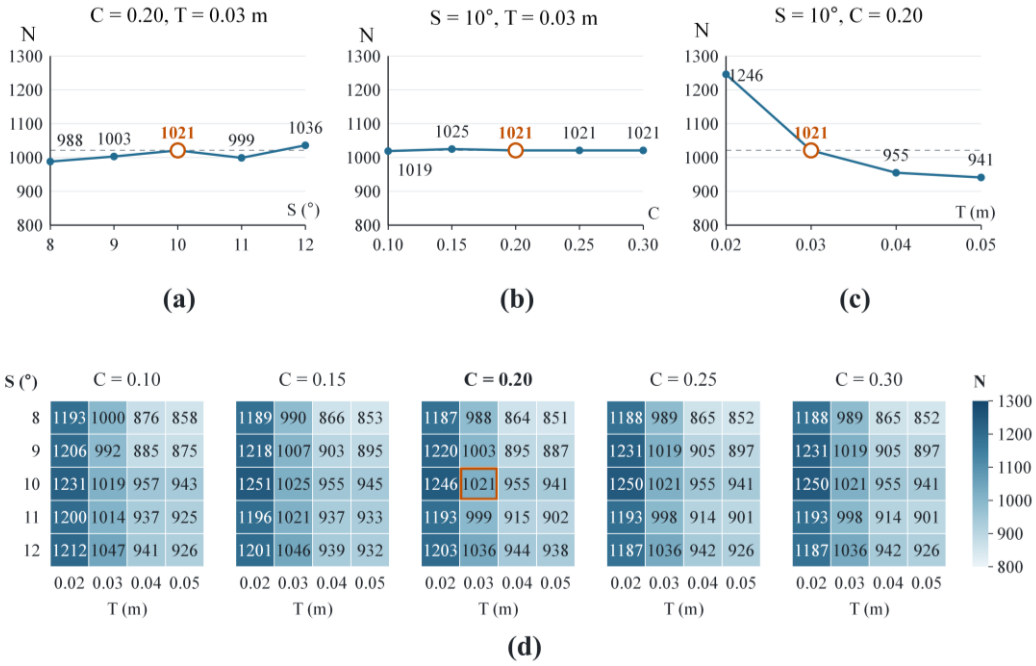

Figure 2. Variation of extracted plane count with segmentation thresholds: (**a**) smoothness threshold S; (**b**) curvature threshold C; (**c**) region-growth threshold T; (**d**) combined sweep of S, C and T. The dashed lines mark the selected parameters (S = 10°, C = 0.20, T = 0.03 m), i.e., the optimal balance point at 1021 planes.

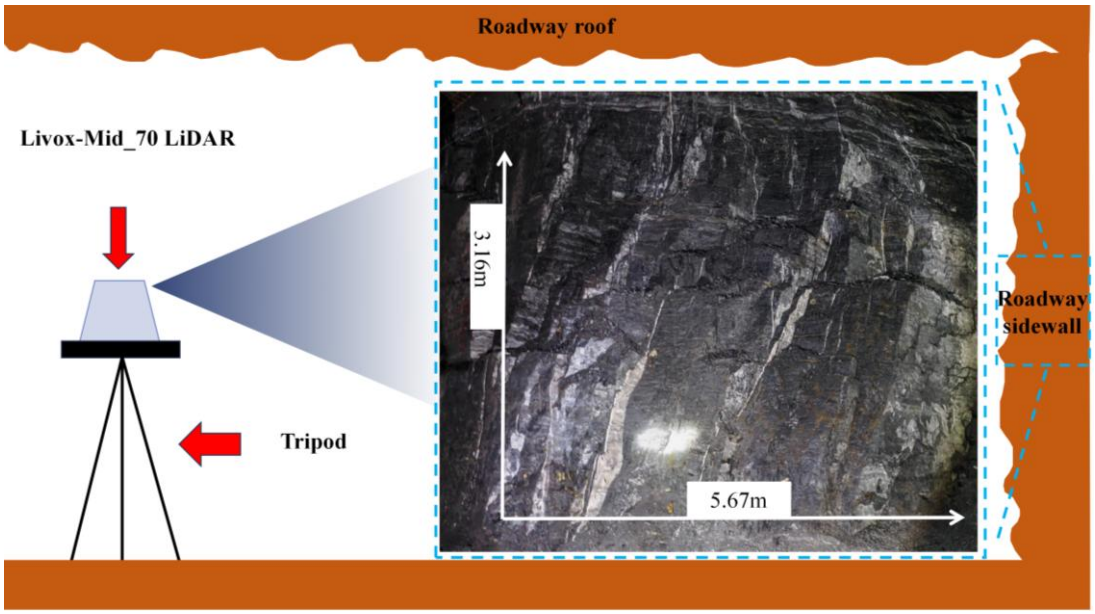

(**a**)

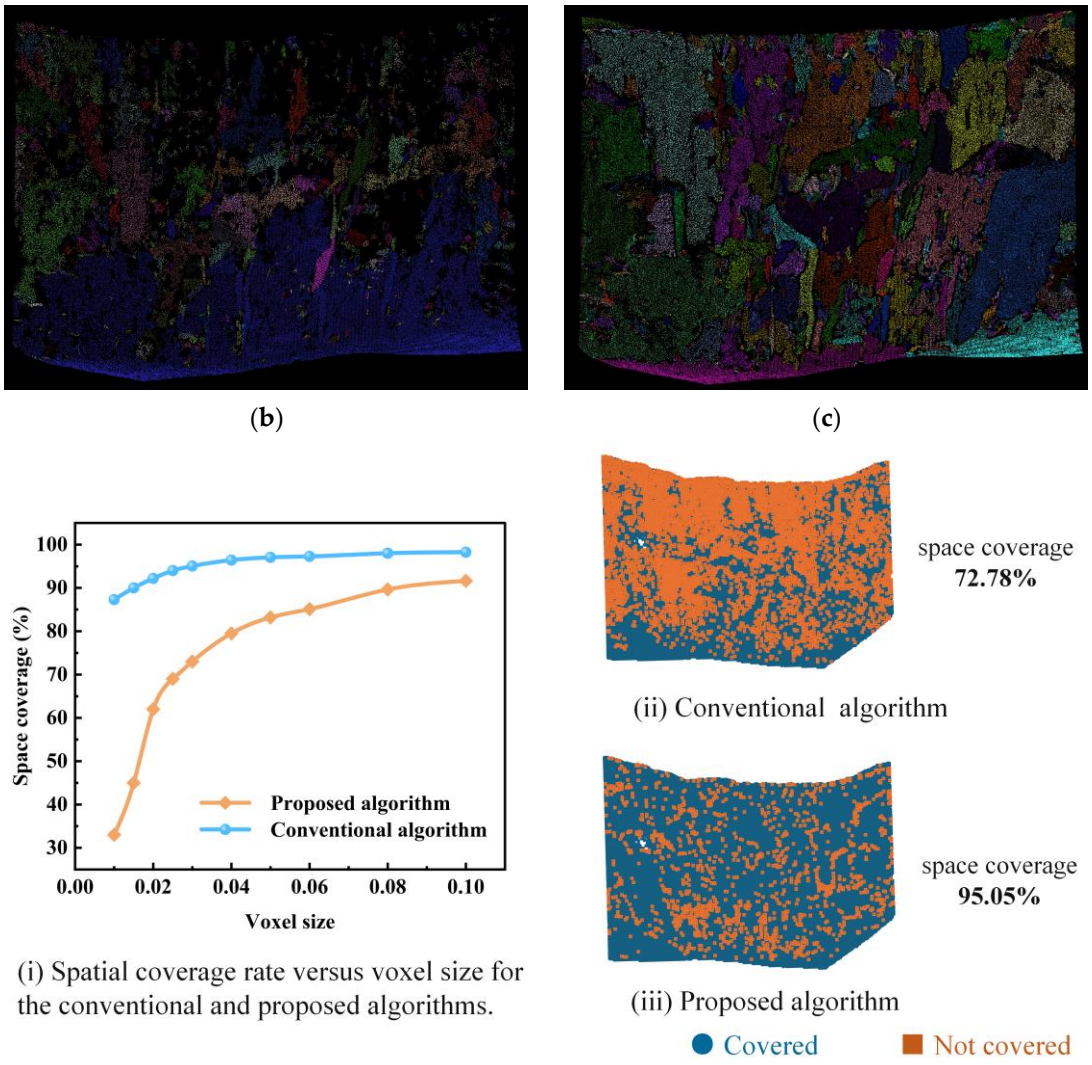

Figure 3. High-precision point cloud acquisition and roughness quantification basis of surrounding rock structural planes in phosphate mine roadway: (**a**) field-scanned point cloud of phosphate mine roadway; (**b**) segmentation results of conventional region-growing algorithm; (**c**) segmentation results of recursive subdivision region-growing algorithm; (**d**) spatial coverage evaluation of structural plane segmentation under varying voxel sizes.

3. Finite-Element Analysis of a Phosphate Mine Roadway Considering Real Rough-Wall Geometry

3.1. Three-Dimensional Reconstruction of Phosphate Mine Roadway Point Cloud Containing Real Rough-Wall Surface

Based on field-measured point cloud data, this study constructs a roadway model with realistic rough sidewalls and establishes corresponding thermo-mechanical coupling conditions, as illustrated in Figure 4:

1. Three-dimensional reconstruction: The Delaunay triangulation algorithm (circumcircle criterion) was applied to generate a non-overlapping triangular mesh and reconstruct the wall surface (Figure 4a). Edge outermost vertices are extracted to build fixed-height contour curves, which are then extended to generate new point clouds. Secondary Delaunay triangulation yields a preliminary geometric model that preserves inherent surface roughness. To reconcile computational efficiency and geo-

metric precision, Poisson surface reconstruction (which fits implicit surfaces via normal vectors and extracts isosurfaces) optimizes the preliminary model and outputs regular meshes with reduced computational overhead (Figure 4b).

2. To isolate the effect of wall roughness on the thermo-elastic response of phosphorite and to minimize the disturbance caused by non-uniform ground stresses, the wall geometry was vertically oriented, thereby reproducing the actual stress and heat-transfer conditions in the underground environment (Figure 4c). The roof and floor were assigned dolomite properties, while phosphorite was assigned to both sidewalls; all material parameters used in the finite-element analysis are summarized in Table 1.
3. A typical mining depth of ~550 m, corresponding to a vertical self-weight stress of 15 MPa calculated by $\sigma_v = \varrho gh$ (where ϱ is rock density, g is gravitational acceleration, and h is overburden depth), serves as the benchmark for characterizing ground stress fields at varying excavation depths. Five ground pressure gradients (9, 15, 24, 33, 42 MPa) are defined. Taking the thickness-weighted average overburden density of phosphorite and dolomite in Table 1, i.e., ϱ = 2850 kg/m^3, and g = 9.81 m/s^2, these stress levels correspond to burial depths of approximately 320, 540, 860, 1180 and 1500 m, respectively, according to $\sigma_v = \varrho gh$.

Table 1. Parameters of finite-element model.

Parameter	Phosphorite	Dolomite
Density (kg/m^3)	2950	2800
Elastic Modulus (GPa)	100	60
Poisson's ratio	0.267	0.25
Coefficient of Thermal Expansion (°C^{-1})	1.20×10^{-5}	1.20×10^{-5}
Thermal Conductivity (W/(m·°C))	7.92	5.23
Specific Heat Capacity (J/(kg·°C))	840	840
Ground Stress (MPa)	9, 15, 24, 33, 42	9, 15, 24, 33, 42

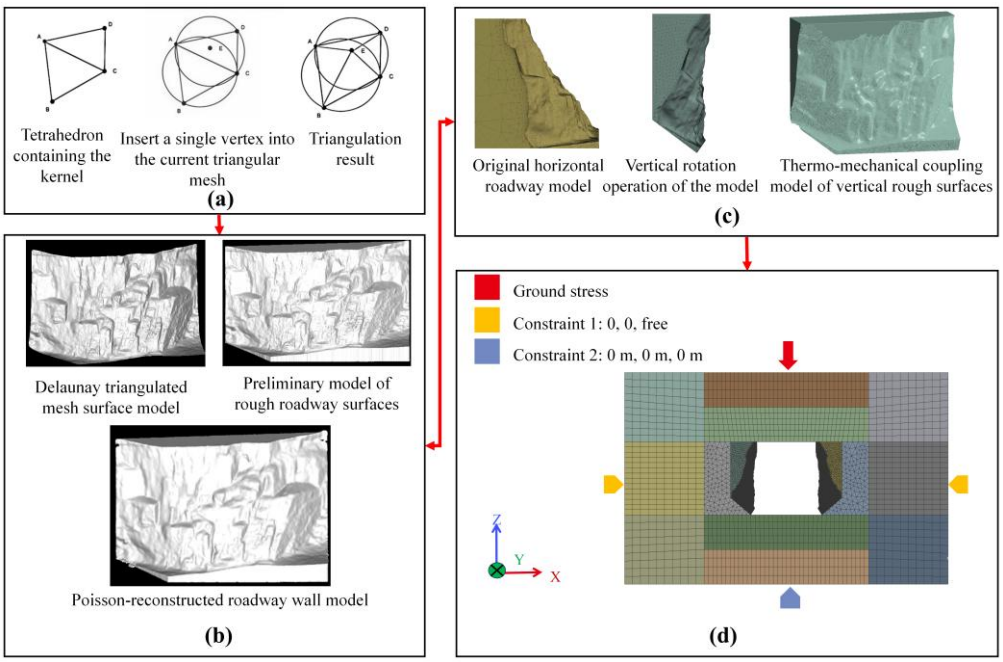

Figure 4. Schematic diagram of roadway rough-wall simulation model construction and thermo-elastic coupling setup: (**a**) generation principle of Delaunay triangular mesh; (**b**) 3D reconstruction

for establishing roadway surface model; (**c**) vertical model of phosphate mine rough walls with mitigated uneven stress distribution; (**d**) boundary conditions of vertical thermo-elastic analysis model for roadways.

The opposite rough wall was generated by mirroring the single-side geometry, and the excavated volume, including the roadway and its safety clearance, was reconstructed. Supplementary geometries were created around the core model using the SCDM (SpaceClaim Design Modeler) sketching tool, and shared topology was adopted to ensure mesh quality at the interfaces. The resulting full-scale 3D roadway model with realistic rough sidewalls measures 21.9 m (X) × 5 m (Y) × 9.87 m (Z). The initial rock temperature was set to 18 °C, with the roadway wall temperature ranging from 15 to 20 °C. In ANSYS workbench 2022 R1, a self-weight stress corresponding to the overburden depth was applied to the roof. The floor was fixed in all three translational directions, while the two sidewalls were constrained horizontally (X and Y) but allowed to deform vertically (Z), thereby replicating the dominant vertical deformation of the surrounding rock mass upon excavation (Figure 4d). Boundary conditions are simplified on purpose to isolate the contribution of surface roughness. Horizontal in situ stresses and excavation-induced stress redistribution are not included in the present model.

3.2. Simulation Results

Thermo-elastic coupling simulations under 15 MPa geostress and corresponding boundary constraints were conducted to acquire the post-excavation stress and temperature fields within surrounding rock (Figure 5). The equivalent stress ranges from 0.20 to 99.03 MPa. High-stress domains (yellow to red) are concentrated in concave areas due to the convergence of force flux, whereas low-stress regions (blue) occur on convex or arched surfaces, where divergent flux induces stress relief. At a simulation time of 1800 s, the rock temperature ranges from 17.998 to 18.099 °C, with a maximum difference of only 0.1 °C. High-temperature zones (red-yellow) coincide with high-stress concentration zones, primarily distributed on the flat roof and local concave depressions; the temperature rise is attributed to the local heat conduction paths being obstructed by the geometric morphology, leading to heat accumulation. Low-temperature zones (blue-green) are mainly located beneath convex wall structures, resulting from low stress levels and favorable heat dissipation conditions. These results indicate that the undulating rough topography of the rock surface governs the local stress field and thermal responses by altering the heat conduction paths. Concave regions act as thermal shelters with restricted heat dissipation, leading to local heat accumulation (high temperature), whereas convex zones are highly exposed to the air, promoting efficient cooling (low temperature). Notably, both the stress and temperature fields exhibit highly heterogeneous spatial patterns with a marked synergistic variation, revealing the intrinsic linkage between elastic and thermal responses in the surrounding rock.

To isolate the effect, the rough-wall model exhibits a relatively uniform, horizontally layered temperature and stress distribution entirely dictated by the boundary conditions. Local temperature peaks of the smooth case only occur at geometric junctions, corresponding to stress concentration at these interfaces. In the central region of the roadway, the temperature of the smooth-wall model stays at approximately 18.072 °C. In stark contrast, the rough-wall model (Figure 5a,b) displays highly heterogeneous spatial patterns; within the same corresponding region, the concave segments reach 18.088–18.099 °C. This direct comparison demonstrates that the observed thermal anomalies and stress concentrations are induced by geometric roughness, which alters local heat conduction paths and force flux, rather than a numerical artifact arising from the prescribed boundary conditions.

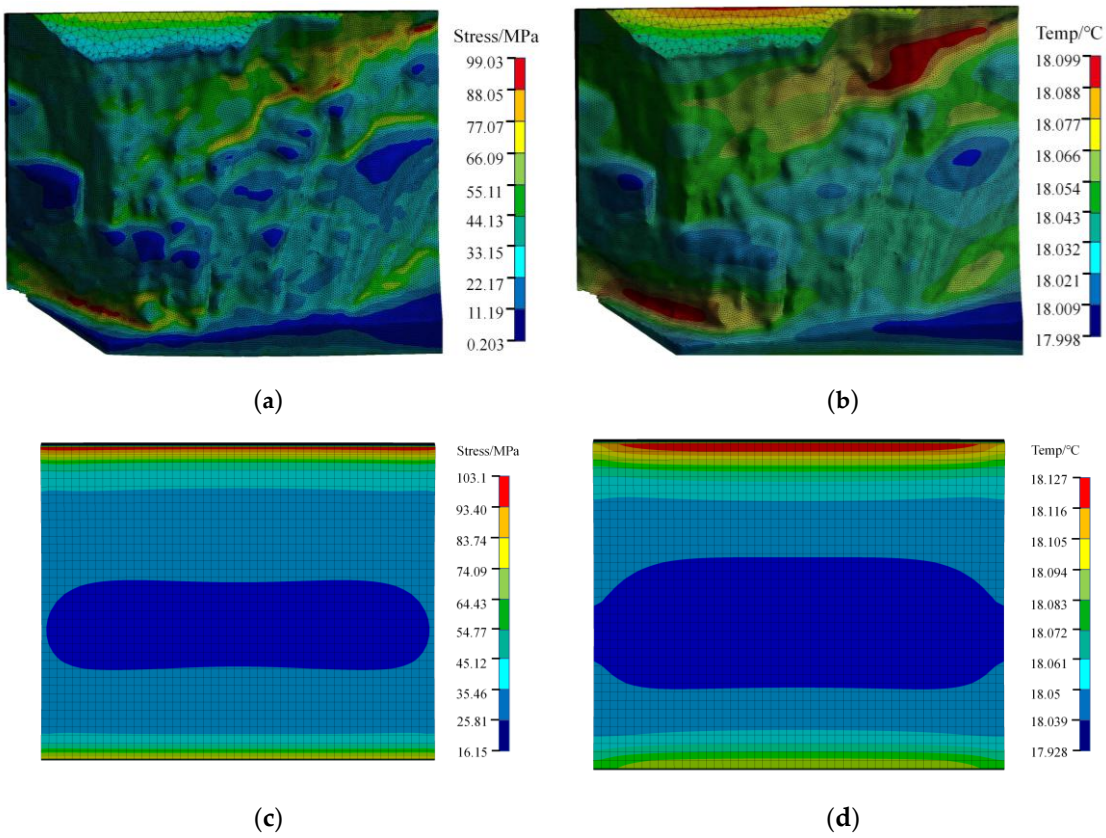

Figure 5. Simulation contours at 15 MPa ground stress: (**a**) contour plot of equivalent stress field under 15 MPa; (**b**) contour plot of temperature field under 15 MPa; (**c**) equivalent stress contour of the smooth-wall model; (**d**) temperature contour of the smooth-wall model.

To quantify how geostress affects thermo-mechanical coupling of surrounding rock, roadway elastic and thermal behaviors were examined at five vertical geostress levels (9, 15, 24, 33, 42 MPa; Figures 6 and 7). As geostress increases, the spatial distribution patterns of the stress and thermal fields remain essentially unchanged, while their magnitudes and affected zones expand simultaneously. Even at 9 MPa, roughness-induced heterogeneity is distinct: geometric discontinuities such as grooves and fractures consistently form coupled high-stress and high-temperature domains. These dominant coupled zones intensify with increasing geostress—roof depressions and local concavities on the right side show progressive stress–thermal amplification from 15 MPa to 42 MPa (Figure 6).

Stress and thermal contours under different geostress levels were processed to extract the evolution curves of characteristic monitoring points, including global extrema, low-temperature Point A (lower-left convex zone), and coupled high-stress/high-temperature Point B (lower-left concave depression). The evolution curves of these points (Figure 7) reveal distinct scaling behaviors. As shown in Figure 7b, the stress amplitude increases almost proportionally with applied geostress. The normalized stress concentration factor $K = \sigma_{max}/P$ (where σ_{max} is the peak equivalent stress and P is the far-field geostress) remains nearly constant at approximately 6.6, indicating linear stress amplification within the pure elastic range. However, as shown in Figure 7a, temperature evolution exhibits a nonlinear response: concave Point B shows a significantly larger temperature increase slope against geostress than convex Point A, demonstrating nonlinear amplification of the thermal gradient.

Two mechanisms account for this nonlinear thermal behavior. First, surface roughness governs the spatial patterns of both stress and temperature: convergent force flux generates stress concentration and temperature rise in concave zones, whereas divergent

flux induces stress relaxation and lower temperatures in convex zones. Although the stress amplitude scales linearly with geostress, the thermal contrast between high- and low-stress domains increases. Second, higher geostress strengthens thermo-elastic coupling via confined heat dissipation: with a constant stress concentration factor, the geometrically constrained heat transfer pathways in concave zones promote heat accumulation, leading to temperature rises that outpace the linear increase in geostress.

Overall, geostress serves as the fundamental driver for the synergistic amplification of stress and thermal fields. The roughness-dominated "concave concentration, convex relaxation" spatial pattern remains unchanged, but the thermal response is nonlinearly amplified under higher geostress: the thermal gradients between high- and low-domain zones are substantially more pronounced at 42 MPa than at 9 MPa. This implies that under high ground stress, irregular concave–convex tunnel surfaces drastically amplify heterogeneous heat accumulation and modify local heat dissipation efficiency, acting as a critical trigger for local thermo-mechanical instability.

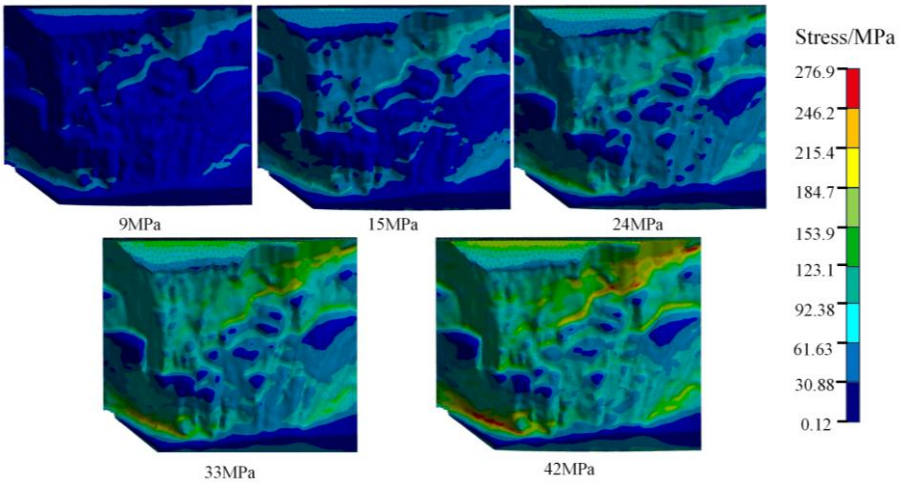

(**a**)

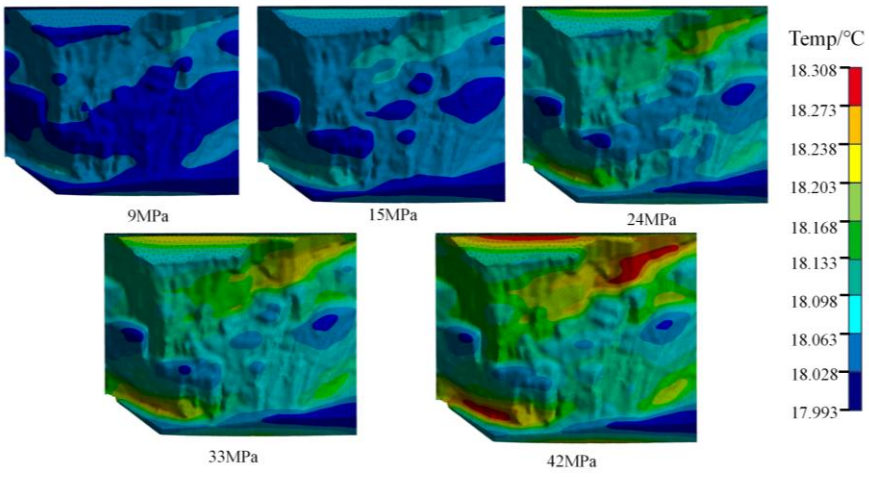

(**b**)

Figure 6. Comprehensive analysis contour plots under different ground stresses: (**a**) equivalent stress field contours under various ground stresses; (**b**) temperature contours under various ground stresses.

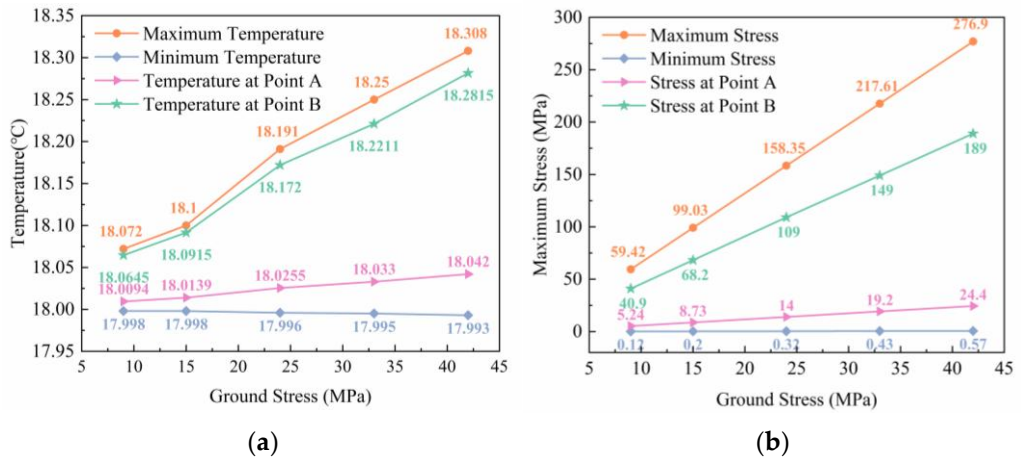

(**a**) (**b**)

Figure 7. Evolution curves of characteristic points: (**a**) variation in wall temperature of phosphate mine with ground stress; (**b**) variation in wall stress of phosphate mine with ground stress.

4. Roughness–Temperature Correlation Model

4.1. Construction of a "Roughness–Stress–Temperature" Coupling Dataset Under Fixed Ground Pressure

As presented in Figure 8, coordinate registration between simulated stress and temperature fields and the 3D scanned point cloud is realized via the ICP algorithm to quantify the formation mechanism of roadway wall-temperature anomalies caused by rough structural planes. Subsequently, the region-growing algorithm is utilized to separate independent structural plane units, and multi-parameter coupling data are extracted for each unit (Figure 9): roughness fractal dimension (D), average infrared temperature (T), average equivalent stress (σ), and ground pressure (P). Among them, the fractal dimension D is used to characterize the roughness degree of the structural plane surface. Its spatial definition is based on the 3D box-counting method: after normalizing the point cloud coordinates within the unit, cover the surface with a cubic grid of side length δ, count the number of non-empty boxes N(δ); change δ (value range 0.005–0.30, step 0.001), fitting the linear part to obtain $D = \lim_{\delta \to 0} \frac{\ln N(\delta)}{\ln(1/\delta)}$. One fractal dimension D is calculated for each segmented unit of the structural surface to guarantee the integrity and comparability of roughness characterization among units. Although the macroscopic wall geometry originates from a single LiDAR reconstruction, the dimensionless parameter D captures local roughness variations over different sub-regions of this surface. The derived stress–thermal relationship thus reveals a general trend to a certain extent.

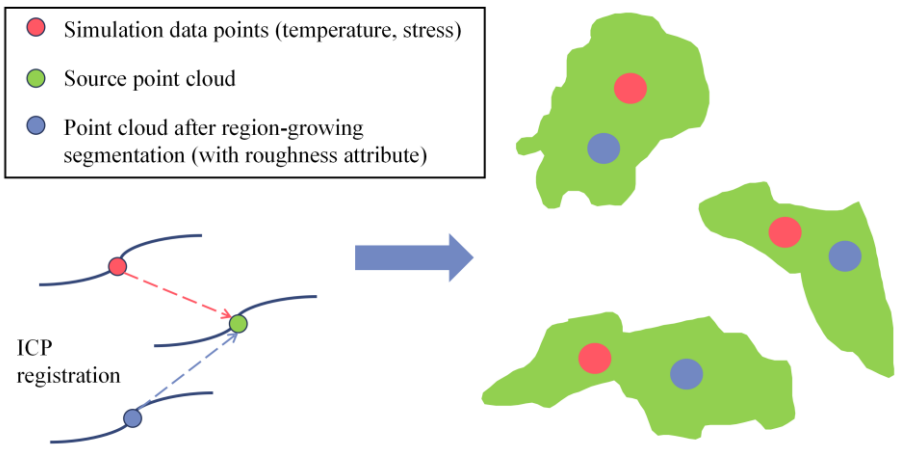

Figure 8. Coupled dataset obtained via ICP registration.

The screening criteria for the regions segmented by the region-growing algorithm included the top 5% hottest regions are retained for analysis, and fragments containing fewer than 533 points are discarded. The largest valid fragment consists of 16,477 points. Ultimately, a multi-parameter dataset comprising 156 groups of "D-T-σ-P" was compiled for subsequent quantitative analysis of the coupled influence mechanisms.

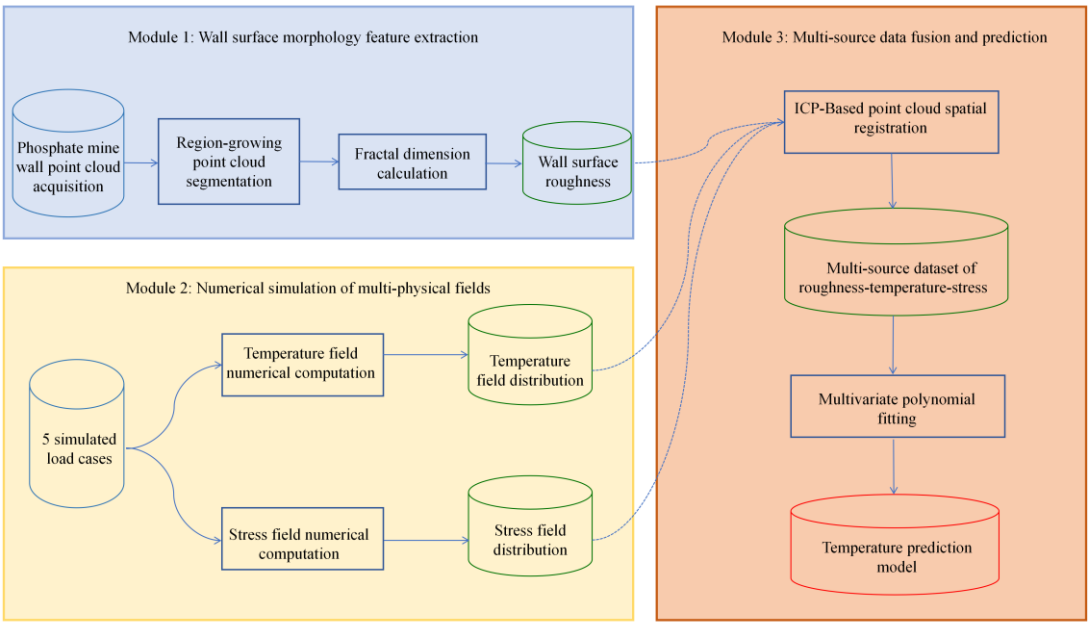

Figure 9. Technical roadmap.

4.2. Multivariate Polynomial Fitting Prediction Model

A roughness–stress predictive model is developed based on 780 datasets obtained from 156 characteristic monitoring points under five geostress levels (i.e., 156 points × 5 stress conditions), covering equivalent stress, fractal roughness dimension, and thermal response data. Equivalent stress σ, fractal dimension D, and geostress P are defined as independent variables, while infrared temperature T serves as the dependent variable. Quadratic and pairwise interaction terms are included. For the final descriptive coefficient table, variables are standardized over the full dataset; the standardized regression is Equation (1). Table 2 reports the standardized coefficients, t-statistics and *p*-values for this model.

$$T_z = \beta_0 + \beta_1\sigma_z + \beta_2 D_z + \beta_3 P_z + \beta_4\sigma_z^2 + \beta_5 D_z^2 + \beta_6 P_z^2 + \beta_7\sigma_z D_z + \beta_8\sigma_z P_z + \beta_9 D_z P_z \quad (1)$$

Regression analysis yields three core conclusions as follows:

1. Stress dominance and energy saturation: The linear coefficient of equivalent stress reaches 0.9868, far exceeding those of other variables, identifying equivalent stress as the strongest statistical correlate of wall thermal responses. This indicates that σ provides the strongest ranking signal among the predictors. Despite the limited absolute accuracy, the standardized coefficients provide a robust ranking of controlling factors. Thermal anomalies are strongly coupled with stress concentration; stress-driven energy accumulation and morphology-mediated heat dissipation govern the wall temperature increments.
2. The positive roughness–stress cross coefficient of 0.0259 quantifies the amplification of thermo-elastic coupling arising from uneven rock surfaces. Rough concave and undulating zones readily induce localized stress concentration and intensified ther-

mal anomalies. This quantitatively supports the interpretation that roughness is associated with nonlinear temperature rise linked to localized stress concentration, which may underpin the "stress–heat dual peaks" observed within concave zones. As presented in Figure 10a, temperatures are distinctly higher within high-stress and high-roughness zones, consistent with the proposed dual-peak mechanism. As illustrated in Figure 10b, stress–temperature curves under various roughness levels reveal that temperature growth from an identical stress increment intensifies as roughness rises. Accordingly, roughness indirectly amplifies thermal responses by magnifying localized stress concentration, rather than acting as a direct thermal source in the coupled thermo-elastic system.

3. Stable roughness regulation under varied geostress: Across geostress boundaries corresponding to different mining depths, roughness maintains a stable regulatory effect on localized stress–thermal responses. Elevated geostress increases overall stress magnitude but does not alter spatial distribution patterns: rough concavities retain high stress and temperature, while convex zones sustain stress relaxation and low temperature; only the amplitude of localized anomalies increases drastically. This reveals that higher geostress merely magnifies the roughness-dominated coupling effect without changing its intrinsic mechanism. The core conclusion is summarized as follows: roughness dominates the spatial localization of thermal anomalies; stress magnitude determines thermal growth amplitude; and rising mining depth (higher geostress) progressively strengthens such distribution patterns.

Table 2. Standardized coefficient estimation results of multivariate nonlinear regression model.

Term Category	Variable	Symbol	Estimated Coefficient	t-Statistic	*p*-Value
Constant term	1	β_0	0.0690	7.18	1.60×10^{-12}
Linear term	Stress	β_1	0.9868	93.68	$<1 \times 10^{-300}$
	Roughness	β_2	0.0281	4.62	4.50×10^{-6}
	Ground stress	β_3	0.0689	7.63	6.96×10^{-14}
Nonlinear term	Stress^2	β_4	−0.1042	−12.16	3.03×10^{-31}
	Roughness^2	β_5	−0.0084	−2.37	0.0179
	Ground stress^2	β_6	−0.0580	−5.87	6.43×10^{-9}
Interaction term	Stress × roughness	β_7	0.0259	4.00	7.02×10^{-5}
	Stress × ground stress	β_8	0.1520	9.69	4.78×10^{-21}
	Roughness × ground stress	β_9	−0.0085	−1.28	0.200

It should be noted that the 780 records correspond to repeated observations of the same 156 independent geometric sites under five geostress levels. Records sharing identical D are grouped into 149 D-value blocks for robust standard error estimation and cross-validation to avoid information leakage.

Within-pressure robustness check: To examine whether the D-associated terms persist within individual stress levels, five pressure-specific six-term models (intercept, σ, D, σ^2, D^2 and σ × D) were fitted separately at P = 9, 15, 24, 33 and 42 MPa (156 records each). Because each subset is standardized independently, these coefficients are not directly comparable with those of the pooled model and are used only as a within-pressure check on the joint significance of the D terms. The three D-containing terms were tested jointly by a block-robust Wald test, and the five resulting *p*-values were Holm-adjusted. All tests remained statistically significant after adjustment (Table 3, adjusted $p = 0.00418 \sim 0.01663$), showing that roughness influences temperature variation across all considered stress levels.

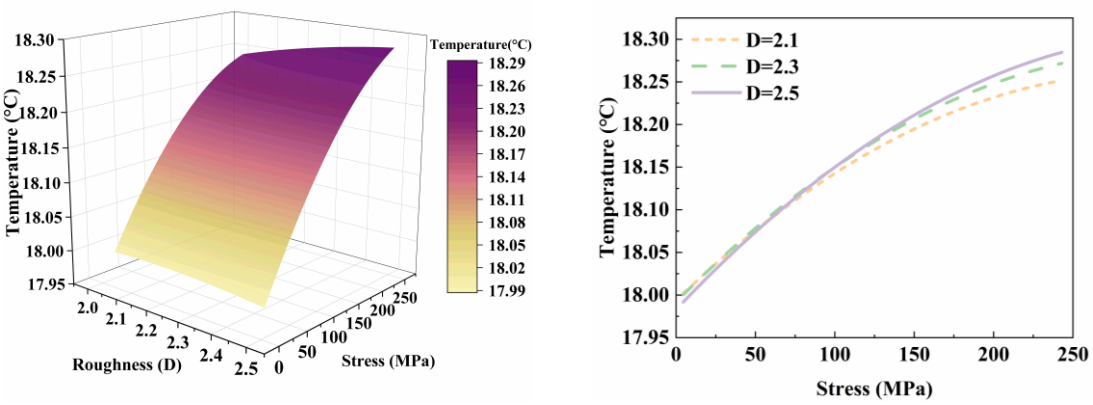

(**a**) (**b**)

Figure 10. Coupling relationship between equivalent stress and temperature response modulated by roughness at P = 24 MPa: (**a**) temperature response surface under roughness–stress interaction; (**b**) stress–temperature response at different roughness levels.

Table 3. Within-pressure joint significance tests for roughness-related terms.

P (MPa)	Joint F for D Terms	Unadjusted *p*	Holm-Adjusted *p*
9	5.851	0.00084	0.00418
15	5.629	0.00111	0.00444
24	4.682	0.00374	0.01121
33	4.060	0.00831	0.01663
42	3.983	0.00918	0.01663

Five-fold grouped out-of-fold validation is adopted, with standardization conducted exclusively within training folds, and predictions back-transformed to °C prior to error calculation. The pressure-specific out-of-fold results are summarized in Table 4 and Figure 11. For the five geostress levels, RMSE ranges from 0.00334 to 0.01496 °C (5.26~5.49% of the within-pressure temperature span), with R^2 between 0.9640 and 0.9662. For the pooled case, RMSE = 0.00966 °C, RMSE/span = 3.26% and (R^2 = 0.9819). This accuracy enables relative thermal-risk assessment and ranking of roughness-linked thermal anomalies. However, as the absolute prediction error can be comparable to or larger than local temperature contrasts caused by roughness, the model is regarded mainly as a trend-and-ranking tool.

In brief, roughness exerts limited direct thermal effects but magnifies thermal anomalies via localized stress concentration. Equivalent stress dominates the overall amplitude of thermal responses. Under variable geostress, roughness-induced localized coupling is enhanced, while its intrinsic spatial pattern stays unchanged. A unified thermo-mechanical coupling framework is therefore proposed: roughness determines anomaly localization, and stress controls thermal growth magnitude. These findings offer theoretical support for infrared thermal anomaly identification and rockburst early warning in deep roadways.

Table 4. Five-fold grouped out-of-fold prediction performance of the five pressure-specific models.

P (MPa)	Observed T (°C)	Span (°C)	RMSE (°C)	RMSE/span	R^2
9	18.0070–18.0704	0.0634	0.00334	5.26%	0.9658
15	18.0102–18.0980	0.0878	0.00479	5.45%	0.9640
24	18.0189–18.1858	0.1669	0.00886	5.31%	0.9662
33	18.0243–18.2383	0.2140	0.01140	5.33%	0.9662
42	18.0309–18.3036	0.2727	0.01496	5.49%	0.9641

Pooled	18.0070–18.3036	0.2966	0.00966	3.26%	0.9819

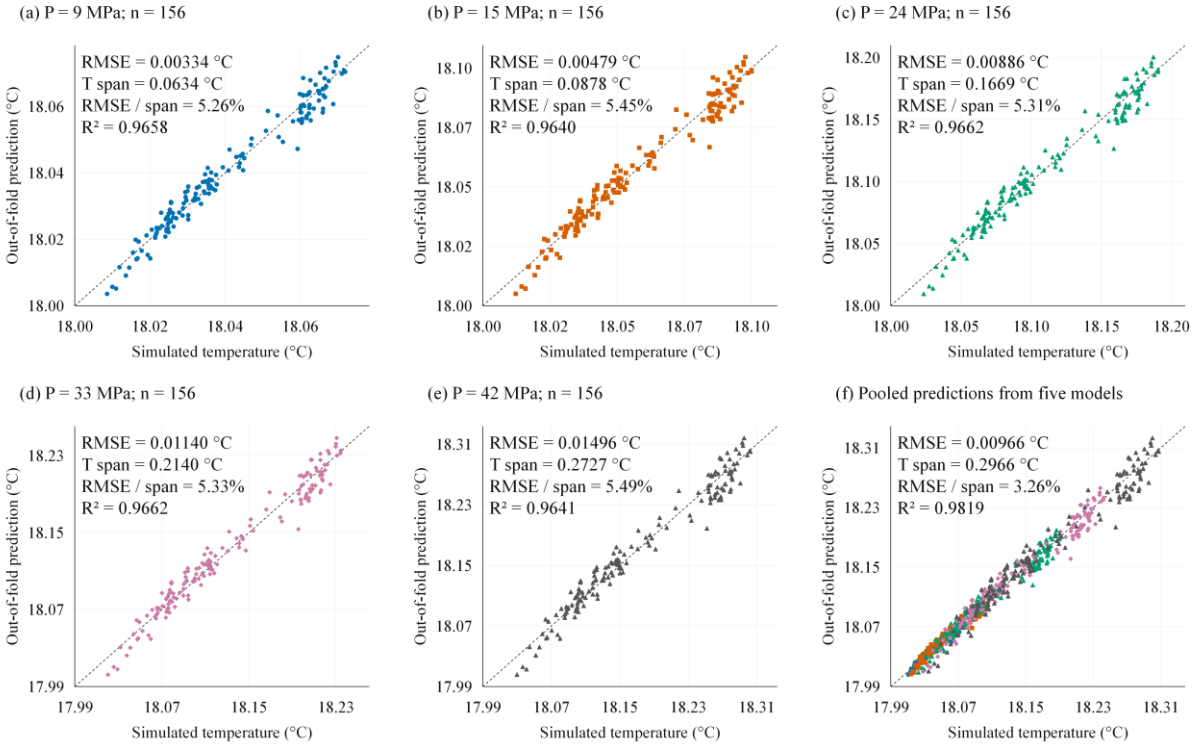

Figure 11. Five-fold grouped out-of-fold predictions from five pressure-specific quadratic models: (**a**–**e**) P = 9, 15, 24, 33 and 42 MPa, respectively; (**f**) pooled predictions from the five models.

5. Conclusions

This study developed an adaptive region-growing algorithm for high-precision segmentation of rough rock structural planes and conducted numerical thermo-mechanical simulations to investigate the role of surface roughness in deep roadway thermal responses. The principal findings are summarized as follows:

1. Surface roughness governs the formation of a stable heterogeneous stress–temperature distribution pattern: concave regions converge force flux, producing high stress and restricted heat dissipation (high temperature), whereas convex regions diverge force flux and are highly exposed, exhibiting stress relaxation and lower temperatures.
2. Rising geostress linearly increases the overall stress amplitude but nonlinearly intensifies the thermal heterogeneity, with concave zones showing higher temperature sensitivity than convex areas.
3. Regression analysis confirms equivalent stress as the strongest statistical correlate and dominant ranking factor for temperature variation, while roughness amplifies this effect via localized stress concentration in concave regions, validating the "roughness-controls-localization, stress-controls-temperature-rise" mechanism.
4. Higher geostress synergistically amplifies roughness-induced thermal effects without altering the fundamental coupling mechanism. Under deep high-stress conditions, irregular tunnel surfaces exacerbate the blocking of local heat conduction paths, amplifying localized heat accumulation and favoring the development of local thermo-mechanical anomalies.
5. These findings establish a quantitative roughness–stress–temperature linkage, providing a theoretical basis for interpreting infrared anomalies and enabling early warning of rockburst hazards.

Author Contributions: Conceptualization, L.S. and Y.L.; methodology, D.C. and L.S.; validation, D.C.; formal analysis, D.C. and M.L.; investigation, D.C. and S.L.; writing—original draft preparation, D.C.; writing—review and editing, D.C., L.S. and Y.L.; supervision, L.S. and Y.L. All authors have read and agreed to the published version of the manuscript.

Funding: This research was funded by the Open Foundation of State Key Laboratory of Green and Efficient Development of Phosphorus Resources (grant number LHKF (2026) 015), the 2025 Hubei Provincial Key Laboratory Directed Commission Project (Basic Research Platform Program, grant number 2025CSA090), the National Natural Science Foundation of China (grant number 52674132), and the Graduate Innovative Fund of Wuhan Institute of Technology (grant number CX2025272).

Institutional Review Board Statement: Not applicable.

Informed Consent Statement: Not applicable.

Data Availability Statement: The datasets and codes used in this study are available on reasonable request from the corresponding author.

Conflicts of Interest: Author Shouqing Li was employed by the company Hubei Xingfa Chemicals Group Co., Ltd., Yichang, China. The remaining authors declare that the research was conducted in the absence of any commercial or financial relationships that could be construed as a potential conflict of interest.

Abbreviations

The following abbreviations are used in this manuscript:

R^2	Coefficient of determination
RMSE	Root-mean-squared error
ROS	Robot operating system
TIR	Thermal infrared radiation
TLS	Terrestrial laser scanning
JRC	Joint roughness coefficient
PCD	Point CLOUD DATA
SCDM	SpaceClaim Design Modeler
kB	kilobytes

References

1. Liu, Z.; Wang, H.; Li, Y.; Wang, X.; Selvadurai, A.P. Triaxial compressive strength, failure, and rockburst potential of granite under high-stress and ground-temperature coupled conditions. *Rock Mech. Rock Eng*. **2023**, *56*, 911–932. https://doi.org/10.1007/s00603-022-03066-5.
2. Waqar, M.F.; Guo, S.; Qi, S. A comprehensive review of mechanisms, predictive techniques, and control strategies of rockburst. *Appl. Sci*. **2023**, *13*, 3950. https://doi.org/10.3390/app13063950.
3. Fan, T.; Zhang, Q.; Wang, X.; Dong, W.; Wang, S.; Li, J. Spray water temperatures effect on surrounding rock stability and rockburst mitigation under high altitude and high temperature conditions. Geotech. *Geol. Eng*. **2025**, *43*, 339. https://doi.org/10.1007/s10706-025-03299-5.
4. Wang, H.; Liu, Z.; Lin, C.; Yang, Q.; Hamdi, E. Non-monotonic effect of differential stress and temperature on mechanical property and rockburst proneness of granite under high-temperature true triaxial compression. *Geomech. Geoenerg. Georessour*. **2024**, *10*, 162. https://doi.org/10.1007/s40948-024-00891-6.
5. Zhang, C.; Feng, X.T.; Zhou, H.; Chen, B.R.; Zeng, X.H. Rockmass damage development following two extremely intense rockbursts in deep tunnels at Jinping II hydropower station, southwestern China. *Bull. Eng. Geol. Environ*. **2013**, *72*, 237–247. https://doi.org/10.1007/s10064-013-0470-y.
6. Li, S.; Kuang, Z.; Xiao, Y.; Qiao, Z.; Yang, W. Rockburst tendency prediction based on an integrating method of combination weighting and matter-element extension theory: A case study in the Bayu Tunnel of the Sichuan-Tibet Railway. *Eng. Geol*. **2022**, *308*, 106796. https://doi.org/10.1016/j.enggeo.2022.106796.

7. Feng, G.L.; Feng, X.T.; Chen, B.R.; Xiao, Y.X.; Zhao, Z.N. Effects of structural planes on the microseismicity associated with rockburst development processes in deep tunnels of the Jinping-II Hydropower Station, China. *Tunn. Undergr. Space Technol*. **2019**, *84*, 273–280. https://doi.org/10.1016/j.tust.2018.11.008.
8. Huang, Z.; Tang, C.; Cai, M. Numerical analysis of unloading-induced rock failure: Insight into strainburst mechanism. *Indian Geotech. J*. **2018**, *48*, 558–563. https://doi.org/10.1007/s40098-017-0260-8.
9. Ren, F.; Gao, Z.; Ma, K.; Yang, S. Rockburst probability early warning method based on integrated infrared temperature and acoustic emission parameters. *Int. J. Rock Mech. Min. Sci*. **2025**, *189*, 106097. https://doi.org/10.1016/j.ijrmms.2025.106097.
10. Xu, L.; Gong, F. Experimental Study of Strain Rockburst considering Temperature Effect: Status-of-the-Art and Prospect. *Shock Vib*. **2021**, *2021*, 8767592. https://doi.org/10.1155/2021/8767592.
11. Zhang, Y.; Xia, Y.; Lin, M.; Wang, Z.; Huang, J.; Yan, Y.; Mei, W. Experimental analysis of structure rockburst in rock-like materials under gradient loading using coupled infrared thermography and acoustic emission. *Rock Mech. Rock Eng*. **2026**, *59*, 8709–8737. https://doi.org/10.1007/s00603-025-05206-z.
12. Liu, P.; Chen, S.; Liu, Q.; Guo, Y.; Ren, Y.; Zhuo, Y.; Feng, J. A potential mechanism of the satellite thermal infrared seismic anomaly based on change in temperature caused by stress variation: Theoretical, experimental and field investigations. *Remote Sens*. **2022**, *14*, 5697. https://doi.org/10.3390/rs14225697.
13. Tian, B.Z.; Liu, S.J.; Zhang, Y.B.; Liang, P.; Liu, X.X. Laboratory simulation of temporospatial evolution characteristics of infrared radiation in the process of rockburst in granite tunnel. *Rock Soil Mech.* **2016**, *37*, 711–718. https://doi.org/10.16285/j.rsm.2016.03.013.
14. Yuan, Z.; Ren, F.; Liu, D. Experimental investigation on the infrared precursors of rockburst in sandstone with different bedding dip angles. *Infrared Phys. Technol.* **2023**, *128*, 104518. https://doi.org/10.1016/j.infrared.2022.104518.
15. Chen, L.; Li, D.J.; Zhang, M.Y.; Shen, M.A.; Gao, Y.; Huo, J.H.; Li, Y.J. Experimental investigation of key infrared radiation signals on rock during damaging process. *Infrared Phys. Technol.* **2022**, *126*, 104320. https://doi.org/10.1016/j.infrared.2022.104320.
16. Wu, Y.H.; Wang, H.P.; Wang, W.; Fan, J.G.; Li, C.M.; Zhang, B.; Sun, D.K.; Hou, F.B. Rockburst failure characteristics and energy evolution law of cross-layer anchored rock mass based on optical-thermal-acoustic combinative monitoring. *Int. J. Min. Sci. Technol.* **2025**, *35*, 2157–2177. https://doi.org/10.1016/j.ijmst.2025.10.005.
17. Sun, C.; Zhuang, L.; Youn, D.J.; Yoon, J.S.; Min, K.B. Laboratory investigation of thermal stresses in fractured granite: Effects of fracture surface roughness and initial stress. *Tunn. Undergr. Space Technol.* **2024**, *145*, 105610. https://doi.org/10.1016/j.tust.2024.105610.
18. Li, Z.W.; Long, M.C.; Xu, P.; Huang, C.Y.; Wang, Y.S. Thermal contact resistance of granite joints under normal stress. *Rock Mech. Rock Eng.* **2023**, *56*, 8317–8338. https://doi.org/10.1007/s00603-023-03450-9.
19. Zhang, Y.; Xia, Y.; Huang, J.; Mei, W.; Lin, M.; Hua, R. Experimental investigation on the fracture process and infrared radiation characteristics of structure rockburst under gradient loading. *Infrared Phys. Technol.* **2024**, *142*, 105565. https://doi.org/10.1016/j.infrared.2024.105565.
20. Lin, M.; Lu, X.; Xia, Y.; Zhang, L.; Liao, Q.; Yang, T. Model experimental investigation on the effects of rockburst on gently inclined structural planes under gradient stresses. *Explos. Shock Waves.* **2025**, *45*, 061442. https://doi.org/10.11883/bzycj-2024-0466.
21. Meng, F.; Zhou, H.; Wang, Z.; Zhang, L.; Kong, L.; Li, S.; Zhang, C.; Hu, S. Experimental study of factors affecting fault slip rockbursts in deeply buried hard rock tunnels. *Bull. Eng. Geol. Environ.* **2017**, *76*, 1167–1182. https://doi.org/10.1007/s10064-016-0926-y.
22. Drews, T.; Miernik, G.; Anders, K.; Höfle, B.; Profe, J.; Emmerich, A.; Bechstädt, T. Validation of fracture data recognition in rock masses by automated plane detection in 3D point clouds. *Int. J. Rock Mech. Min. Sci.* **2018**, *109*, 19–31. https://doi.org/10.1016/j.ijrmms.2018.06.023.
23. Shintassova, M.; Sepulveda, S.A. Estimating joint properties from drill cores using 3D scanning technology. *Geotech. Geol. Eng.* **2025**, *43*, 230. https://doi.org/10.1007/s10706-025-03183-2.
24. Barton, N. Review of a new shear-strength criterion for rock joints. *Eng. Geol*. **1973**, *7*, 287–332. https://doi.org/10.1016/0013-7952(73)90013-6.
25. Kulatilake, P.H.S.W.; Ankah, M.L.Y. Rock Joint Roughness Measurement and Quantification—A Review of the Current Status. *Geotechnics* **2023**, *3*, 116–141. https://doi.org/10.3390/geotechnics3020008.
26. Zhou, H.W.; Xie, H.P.; Kwasniewski, M.A. Cube covering method for fractal dimension calculation of rough surfaces. *Tribology* **2000**, *20*, 455–459.

27. Li, M.; Zhang, Y.; Wang, Y. Evaluation of the Consistency of Rock Joint Surface Morphology Based on Grayscale Surface-Differential Box Counting and Mechanical Tests. *Buildings* **2025**, *15*, 3861. https://doi.org/10.3390/buildings15213861.

Disclaimer/Publisher's Note: The statements, opinions and data contained in all publications are solely those of the individual author(s) and contributor(s) and not of MDPI and/or the editor(s). MDPI and/or the editor(s) disclaim responsibility for any injury to people or property resulting from any ideas, methods, instructions or products referred to in the content.